

Air Force Institute of Technology

**AFIT Scholar**

---

Faculty Publications

---

3-2020

## **Infrared-active Phonon Modes in Single-crystal Thorium Dioxide and Uranium Dioxide**

Sean Knight

Rafał Korlacki

Christina L. Dugan

James C. Petrosky

Alyssa Mock

*See next page for additional authors*

Follow this and additional works at: <https://scholar.afit.edu/facpub>



Part of the [Atomic, Molecular and Optical Physics Commons](#), and the [Semiconductor and Optical Materials Commons](#)

---

---

**Authors**



Sean Knight, Rafał Korlacki, Christina L. Dugan, James C. Petrosky, Alyssa Mock, Peter A. Dowben, J. Matthew Mann, Martin M. Kimani, and Mathias Schubert

---

# Infrared-active phonon modes in single-crystal thorium dioxide and uranium dioxide

Cite as: J. Appl. Phys. **127**, 125103 (2020); <https://doi.org/10.1063/1.5143724>

Submitted: 07 January 2020 . Accepted: 04 March 2020 . Published Online: 23 March 2020

 Sean Knight,  Rafał Korlacki, Christina Dugan, James C. Petrosky,  Alyssa Mock,  Peter A. Dowben, J. Matthew Mann, Martin M. Kimani, and  Mathias Schubert



View Online



Export Citation



CrossMark

## ARTICLES YOU MAY BE INTERESTED IN

[Band-to-band transitions and critical points in the near-infrared to vacuum ultraviolet dielectric functions of single crystal urania and thoria](#)

Applied Physics Letters **114**, 211901 (2019); <https://doi.org/10.1063/1.5087059>

[Infrared active phonons in monoclinic lutetium oxyorthosilicate](#)

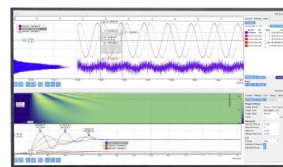
Journal of Applied Physics **127**, 115702 (2020); <https://doi.org/10.1063/1.5135016>

[Thermal transport across nanoscale damage profile in sapphire irradiated by swift heavy ions](#)

Journal of Applied Physics **127**, 035108 (2020); <https://doi.org/10.1063/1.5126413>

Challenge us.

What are your needs for  
periodic signal detection?



Zurich  
Instruments

# Infrared-active phonon modes in single-crystal thorium dioxide and uranium dioxide

Cite as: J. Appl. Phys. 127, 125103 (2020); doi: 10.1063/1.5143724

Submitted: 7 January 2020 · Accepted: 4 March 2020 ·

Published Online: 23 March 2020



Sean Knight,<sup>1,a)</sup> Rafal Korlacki,<sup>1</sup> Christina Dugan,<sup>2</sup> James C. Petrosky,<sup>2</sup> Alyssa Mock,<sup>1</sup> Peter A. Dowben,<sup>3</sup> J. Matthew Mann,<sup>4</sup> Martin M. Kimani,<sup>4,5</sup> and Mathias Schubert<sup>1,6,7</sup>

## AFFILIATIONS

<sup>1</sup>Department of Electrical and Computer Engineering, University of Nebraska-Lincoln, Lincoln, Nebraska 68588, USA

<sup>2</sup>Air Force Institute of Technology, Wright-Patterson Air Force Base, Ohio 45433-7765, USA

<sup>3</sup>Department of Physics and Astronomy, University of Nebraska-Lincoln, Lincoln, Nebraska 68588, USA

<sup>4</sup>Air Force Research Laboratory, Sensors Directorate, Wright Patterson AFB, Ohio 45433, USA

<sup>5</sup>KBRwyle, Dayton, Ohio 45431, USA

<sup>6</sup>Terahertz Materials Analysis Center, Department of Physics, Chemistry and Biology (IFM), Linköping University, SE 58183, Linköping, Sweden

<sup>7</sup>Leibniz Institute for Polymer Research, 01069 Dresden, Germany

<sup>a)</sup>Author to whom correspondence should be addressed: sean.knight@engr.unl.edu. URL: <http://ellipsometry.unl.edu/>

## ABSTRACT

The infrared-active phonon modes, in single-crystal samples of thorium dioxide (ThO<sub>2</sub>) and uranium dioxide (UO<sub>2</sub>), were investigated using spectroscopic ellipsometry and compared with density functional theory. Both ThO<sub>2</sub> and UO<sub>2</sub> are found to have one infrared-active phonon mode pair [consisting of one transverse optic (TO) and one associated longitudinal optic (LO) mode], which is responsible for the dominant features in the ellipsometric data. At room temperature, our results for the mode pair's resonant frequencies and broadening parameters are comparable with previous reflectance spectroscopy characterizations and density functional theory predictions. For ThO<sub>2</sub>, our ellipsometry and density function theory results both show that the LO mode broadening parameter is larger than the TO mode broadening. This signifies mode anharmonicity, which can be attributed to the intrinsic phonon-phonon interaction. In addition to the main mode pair, a broad low-amplitude impurity-like vibrational mode pair is detected within the reststrahlen band for both ThO<sub>2</sub> and UO<sub>2</sub>. Elevated temperature measurements were performed for ThO<sub>2</sub> in order to study the mechanisms by which the phonon parameters evolve with increased heat. The observed change in the TO resonant frequency is in excellent agreement with previous density functional calculations, which only consider volume expansion of the crystal lattice. This suggests that the temperature-dependent change in the TO frequency is primarily due to volume expansion. The change in the main mode pair's broadening parameters is nearly linear within the temperature range of this study, which indicates the intrinsic anharmonic scattering (via cubic anharmonicities) as the main decay mechanism.

Published under license by AIP Publishing. <https://doi.org/10.1063/1.5143724>

## I. INTRODUCTION

Due to their importance to nuclear fuel rods, thorium dioxide (ThO<sub>2</sub>) and uranium dioxide (UO<sub>2</sub>) have been the subject of many scientific investigations.<sup>1,2</sup> Heat transfer, fuel expansion, and related physical properties are of particular interest for fuel rods used in nuclear power plants,<sup>3</sup> where heat must be transferred from the core of the fuel rod to the outer surface. Because ThO<sub>2</sub> and UO<sub>2</sub> have low thermal conductivity, a better microscopic understanding of lattice vibrations may help with designing improved thermal

conductivity properties. This is all the more important because there are conflicting reports on whether the infrared-active (IR) phonon modes significantly contribute to heat transfer.<sup>3,4</sup> ThO<sub>2</sub> may be blended with UO<sub>2</sub> to improve fuel rod efficiencies.<sup>5</sup> Therefore, accurate measurement of the IR-active phonon modes of ThO<sub>2</sub> and UO<sub>2</sub> is a prerequisite for improvement of heat transport properties.

In order to fully characterize the IR-active modes, the complex-valued IR dielectric function  $\epsilon(\omega)$  must be determined from optical measurements. From the spectral behaviors of  $\text{Re}\{\epsilon(\omega)\}$  and

$\text{Im}\{\varepsilon(\omega)\}$ , physically meaningful parameters can be extracted, such as phonon mode frequency, amplitude, and broadening parameters.<sup>6</sup> So far, only IR reflectance (intensity) spectroscopy has been used to optically characterize IR-active phonon modes in  $\text{ThO}_2$  and  $\text{UO}_2$ .<sup>7–10</sup> This approach relies either on Kramers–Kronig transforms to obtain both  $\text{Re}\{\varepsilon(\omega)\}$  and  $\text{Im}\{\varepsilon(\omega)\}$  or relies on best-match model calculations using reflectance data as a model target with a predetermined parameterized model for  $\varepsilon(\omega)$ . In contrast to reflectance spectroscopy, spectroscopic ellipsometry (SE) measures two quantities (relative amplitude and relative phase shift between *s*- and *p*-polarized light after reflection) instead of just one quantity (reflectivity). This additional information allows  $\text{Re}\{\varepsilon(\omega)\}$  and  $\text{Im}\{\varepsilon(\omega)\}$  to be extracted independently from each other or can facilitate more accurate best-match model calculations targeting two independent spectra of the ellipsometric data using a predetermined parameterized model.

In this work, we employed IR spectroscopic ellipsometry (IRSE) to extract the dielectric functions of  $\text{ThO}_2$  and  $\text{UO}_2$ . Our approach allows us to characterize their IR phonon modes. We compare our results with density functional theory (DFT) calculations and previous reflectance spectroscopy. The existence of an IR-active impurity-like vibrational mode pair is discussed, as well as its possible anharmonic coupling to other phonon modes. For  $\text{ThO}_2$ , variable temperature measurements were performed in order to investigate the variation of the phonon mode parameters with the increase in the sample volume at elevated temperatures.

## II. THEORY

### A. Spectroscopic ellipsometry

Spectroscopic ellipsometry is a measurement technique, which quantifies the change in the polarization of light  $\tilde{\rho}$  after interaction with a sample.<sup>6,11,12</sup> In the case of reflection, the change in polarization can be written as

$$\tilde{\rho} = \frac{\tilde{r}_p}{\tilde{r}_s} = \tan(\Psi)e^{i\Delta}, \quad (1)$$

where  $\tilde{r}_p$  and  $\tilde{r}_s$  are the complex-valued Fresnel reflection coefficients for light polarized parallel (*p*) and perpendicular (*s*) to the plane of incidence. At each frequency, a ( $\Psi$ ,  $\Delta$ ) pair is measured, where  $\Psi$  is rotation of the light's polarization state (about its axis of propagation) and  $\Delta$  is the relative phase shift between the *p* and *s* components.

### B. Optical model approach

To extract physically meaningful quantities from SE data ( $\Psi$ ,  $\Delta$ ), an appropriate optical model must be implemented. The optical model used here consists of ambient air, a surface roughness layer, and bulk single-crystal  $\text{ThO}_2$  or  $\text{UO}_2$ , where all constituents meet at plane parallel interfaces. The dielectric function for the surface roughness layer ( $\varepsilon_{\text{rough}}$ ) is calculated by averaging the ambient air ( $\varepsilon_{\text{air}} = 1$ ) and bulk ( $\varepsilon_{\text{bulk}}$ ) dielectric functions, via  $\varepsilon_{\text{rough}} = (1 + \varepsilon_{\text{bulk}})/2$ . For the  $\text{ThO}_2$  sample, a small silver contact (1% surface area coverage) must be included in the optical model to account for the metallic

reflectivity of a small electric contact, which was furnished onto the sample.

For the temperature and spectral range investigated here, the dominant contributions to  $\varepsilon(\omega)$  come from IR-active phonon modes. The optical response of IR-active phonon modes can be modeled using anharmonic broadened Lorentz oscillators,<sup>6</sup> which can be cast into the so-called four-parameter semi-quantum (FPSQ) model.<sup>13</sup> The FPSQ model was motivated by Gervais and Piriou permitting for different phonon decay times of LO and TO modes in crystals with multiple branches of phonon modes. By allowing for independent damping parameters of TO and LO modes, anharmonic effects in multiple (polar) phonon-mode materials can be modeled.<sup>13–16</sup> We used the following model dielectric function to describe  $\varepsilon$ :

$$\varepsilon(\omega) = \varepsilon_\infty \prod_{i=1}^N \frac{\omega_{\text{LO},i}^2 - \omega^2 - i\omega\gamma_{\text{LO},i}}{\omega_{\text{TO},i}^2 - \omega^2 - i\omega\gamma_{\text{TO},i}}. \quad (2)$$

Here, index *i* specifies the phonon mode pair number and *N* is the total number of mode pairs. Corresponding to every phonon mode pair is a lattice resonance with transverse optic (TO) and longitudinal optic (LO) character. To avoid confusion, we refer to each term in Eq. (2) as “mode pairs” (*i* = 1, 2, ...) and their corresponding TO and LO components as just “modes.” The parameters  $\omega_{\text{TO}}$ ,  $\gamma_{\text{TO}}$ ,  $\omega_{\text{LO}}$ ,  $\gamma_{\text{LO}}$ , and  $\varepsilon_\infty$  are the resonant frequency and broadening of the TO resonance, resonant frequency and broadening of the LO resonance, and high frequency dielectric constant, respectively. Anharmonic phonon interactions may comprise, for example, optical phonon decays into acoustic phonons (by cubic or quartic anharmonicities).<sup>17</sup>

### C. Density functional theory calculations

Theoretical calculations of long wavelength active  $\Gamma$ -point phonon frequencies were performed by plane wave density functional theory (DFT) using Quantum ESPRESSO (QE).<sup>18</sup> We used the generalized gradient approximation (GGA) exchange-correlation functional of Perdew, Burke, and Ernzerhof (PBE)<sup>19</sup> and ultrasoft pseudopotentials from the PSLibrary version 1.0.<sup>20</sup> The valence configuration for thorium used here is  $[\text{Rn}] 5f^{0.5} 6d^{1.5} 7s^2$ . The standard *fcc* fluorite structures were first relaxed to force levels less than  $10^{-5}$  Ry bohr<sup>-1</sup>. A regular shifted  $8 \times 8 \times 8$  Monkhorst–Pack grid was used for sampling of the Brillouin zone.<sup>21</sup> A convergence threshold of  $10^{-12}$  Ry was used to reach self consistency with large electronic cutoffs of 110 Ry for the wavefunction and 1000 Ry for the charge density. The structural relaxation yielded lattice constants of 5.61 Å for  $\text{ThO}_2$  and 5.37 Å for  $\text{UO}_2$ . The fully relaxed cells were used for subsequent DFT phonon calculations.<sup>22</sup>

According to Born and Huang,<sup>24</sup> the lattice dynamic properties in crystals are categorized under different electric field **E** and dielectric displacement **D** conditions.<sup>25</sup> Specifically, **E** = 0 and **D** = 0 define the transverse optical (TO) modes, associated with the dipole moment. **E** ≠ 0 but **D** = 0 define the longitudinal optical (LO) modes. The latter can be obtained using Born effective charges calculated by the QE's phonon code.<sup>26</sup> Thus, the parameters of the TO modes are obtained as eigenvalues and eigenvectors of the dynamic matrix without the electric-field effects. The parameters of the LO

modes were obtained by adding so-called non-analytical terms to the dynamic matrix in appropriate crystal directions. In cubic crystals, the tensors of Born effective charges are isotropic, which leads to the same eigenvector being the solution for both the TO and LO mode as shown in Fig. 1. From the point of view of DFT, a low bandgap  $\text{UO}_2$  is a semimetal, which makes the calculations of Born effective charges (and any other electric-field-related properties) problematic at this particular level of theory. Therefore, we focused on calculations of phonon properties of  $\text{ThO}_2$ . It is worth noting, however, that due to the similarity of the crystal structure and the atomic mass, the lattice dynamical properties of  $\text{ThO}_2$  are expected to be qualitatively valid for  $\text{UO}_2$  as well. In addition to the  $\Gamma$ -point phonons, the dynamical matrices were calculated over a regular  $8 \times 8 \times 8$  grid in the first Brillouin zone. They were used to produce real-space interatomic force constants, which in turn were used to plot the complete phonon dispersion along a high symmetry path through the first Brillouin zone, shown in Fig. 2.

The fluorite crystal structure with three atoms in the primitive cell possesses nine phonon modes, three acoustic modes, and six optical modes. The optical phonon modes further divide into three

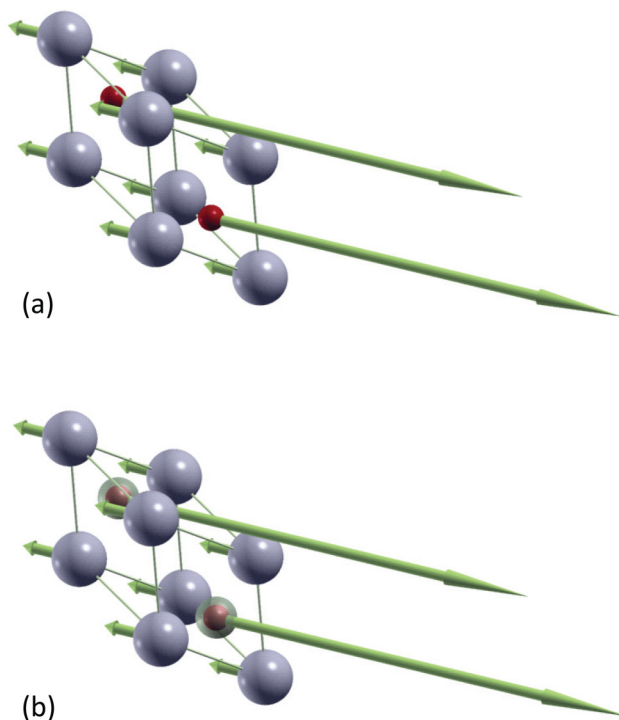


**FIG. 1.** Examples of TO (a) and the corresponding LO (b) modes for  $\text{ThO}_2$  are shown for the primitive unit cell. Please note that the modes, i.e., the atomic displacement patterns, are exactly the same for these two modes. As described in the text, the TO mode is an eigenvector of the dynamic matrix of interatomic force constants. The LO mode was obtained by adding the non-analytical terms to the dynamic matrix in the direction of the transition dipole of the TO. Semi-transparent isosurfaces of the electron charge density are shown around the oxygen atoms in (b).

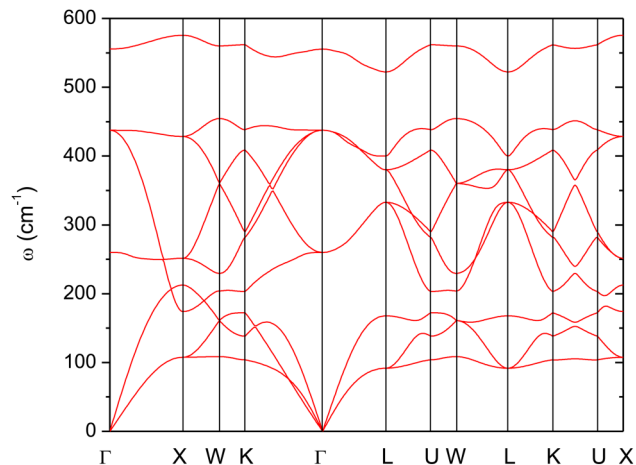


**FIG. 2.** The phonon dispersion along a high symmetry path in the Brillouin zone for  $\text{ThO}_2$ . Labeling of high symmetry points as in Ref. 23.

triply degenerated IR-active modes and three triply degenerated Raman-active modes. Partial charges on the atoms are quantified in terms of the Born effective-charge tensors, i.e., mixed second-order derivatives with respect to atomic displacement and electric field.<sup>26</sup> For  $\text{ThO}_2$ , the Born effective-charge tensors are isotropic, and the positive charge on thorium equals the sum of negative charges on both oxygen atoms. Thus, the electric field adds to the restoring force of the mode, which results in the higher frequency of the LO mode, while the eigenvector direction of the dynamic matrix does not change. The LO mode is the highest frequency branch in the phonon dispersion plot (between  $500$  and  $600 \text{ cm}^{-1}$ ). Figure 1 shows renderings of atomic displacements for TO and LO modes as examples prepared using XCrystDen<sup>27</sup> running under Silicon Graphics Irix 6.5.

In order to verify the general trends of energy and broadening of the TO and LO phonon modes, we performed anharmonic calculations using the D3Q code integrated with the QE distribution.<sup>28–30</sup> Due to the limitations of the code (only implemented for norm-conserving pseudopotentials) for these calculations, we used Hamann–Schlüter–Chiang–Vanderbilt (HSCV)<sup>31</sup> pseudopotentials and the Perdew–Zunger (PZ)<sup>32</sup> local density approximation exchange–correlation functional. The calculations were performed on a regular shifted  $6 \times 6 \times 6$  Monkhorst–Pack grid with a large cutoff of 200 Ry for the wavefunction. These parameters were tested and seen to provide convergence of the harmonic phonon frequencies to the level of  $0.1 \text{ cm}^{-1}$ . The structure was again fully relaxed using the same criteria as for the GGA calculations described above, and the subsequent phonon calculations (second-order harmonic and third order anharmonic) were performed on a regular  $8 \times 8 \times 8$  grid in the first Brillouin zone. The resulting anharmonic dynamical matrices were used to compute the intrinsic phonon–phonon interactions, i.e., widths and energies of phonon modes as a function of temperature in the temperature range of 0 K–800 K. The calculations were performed at a small displacement ( $1 \times 10^{-5}$  of the reciprocal lattice vector) from the  $\Gamma$  point, on a  $200 \times 200 \times 200$  regular



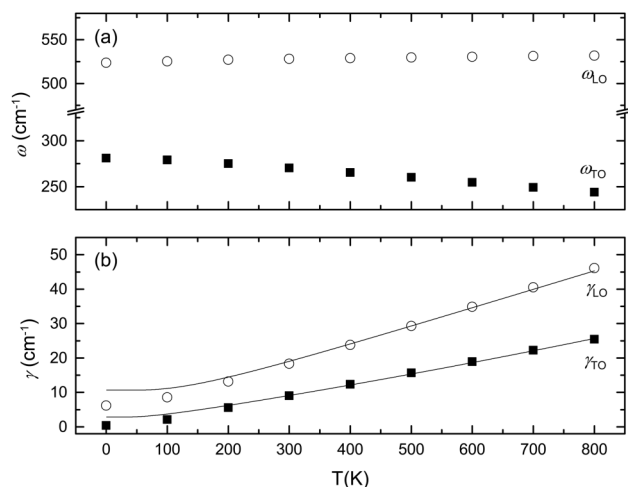


**FIG. 3.** Results of the anharmonic DFT calculations for energy (a) and broadening parameters (b) of TO and LO phonon modes as a function of temperature. Solid lines in (b) are fits to Eq. (4). The resulting best-match model fit parameters are given in the text.

unshifted grid, and with the Gaussian smearing parameter of  $10 \text{ cm}^{-1}$ . The results are presented in Fig. 3.

### III. EXPERIMENT

#### A. Crystal growth

Hydrothermal synthesis was used to grow the  $\text{ThO}_2$  and  $\text{UO}_2$  single-crystals investigated in this work.<sup>33,34</sup> Similar growth procedures were implemented for both  $\text{ThO}_2$  and  $\text{UO}_2$ . The mineralizer solution for both growth reactions was a 6M cesium fluoride solution (Alfa Aesar, 99.99%). Growth reactions were contained in sealed silver ampoules (99.95% Ag, Refining Systems, Inc.).

For the  $\text{ThO}_2$  single-crystal, a  $\text{ThO}_2$  seed crystal was suspended in the upper end of the silver ampoule on a silver seed rack. A charge of  $\text{ThO}_2$  nutrient/feedstock (99.99% thorium oxide, International Bio-analytical Laboratories) was placed into the lower end of the tube, with a porous silver baffle separating the feedstock and the seed crystal. The silver tubes were then placed in a 250 ml Inconel autoclave. Band heaters were installed on the autoclave to form two temperature zones (feedstock and seed crystal zones). The dissolution zone temperature was  $650^\circ\text{C}$  and the crystallization zone was  $600^\circ\text{C}$ . This generated a pressure of 172 MPa. These conditions were maintained for 90 days.

The  $\text{UO}_2$  single-crystal was also grown on a  $\text{ThO}_2$  seed crystal. The mineralizer solution, temperatures, and pressures were the same for the  $\text{UO}_2$  (99.998% uranium oxide, International Bio-analytical Laboratories) growth procedure. However, the growth was only maintained for 50 days.

Both crystals were ground down to the (100) surface (3000 grit, Ultra Tec V5 faceting machine) and polished ( $0.10 \mu\text{m}$  diamond slurry applied to a ceramic lap). The final dimensions of the  $\text{ThO}_2$

single-crystal are  $12 \times 6 \times 1 \text{ mm}^3$ . The dimensions of the  $\text{UO}_2$  single-crystal are  $5 \times 5 \times 1 \text{ mm}^3$ .

#### B. Ellipsometric measurements

Spectroscopic ellipsometry, in the reflection mode, was the measurement technique employed here. For the room temperature measurements on  $\text{ThO}_2$  and  $\text{UO}_2$ , the ellipsometric parameters  $\Psi$  and  $\Delta$  were measured from  $100 \text{ cm}^{-1}$  to  $7000 \text{ cm}^{-1}$  with a resolution of  $2 \text{ cm}^{-1}$ . Data from  $100 \text{ cm}^{-1}$  to  $400 \text{ cm}^{-1}$  were acquired using a home-built Fourier transform-based far-infrared ellipsometer.<sup>35</sup> Data from  $400 \text{ cm}^{-1}$  to  $7000 \text{ cm}^{-1}$  were acquired using a commercially available Fourier transform-based mid-infrared ellipsometer (IR-VASE, J.A. Woollam Co., Inc.). These measurements were performed at three angles of incidence ( $\Phi_a = 50^\circ, 60^\circ,$  and  $70^\circ$ ). The WVASE software (J.A. Woollam Co., Inc.) was used to acquire and analyze all data. All measurements were performed in an open air environment.

For  $\text{ThO}_2$ , additional variable temperature measurements were taken from 293 K to 648 K in increments of 25 K. These were performed using only the far-infrared ellipsometer.<sup>35</sup>  $\Psi$  and  $\Delta$  were measured from  $100 \text{ cm}^{-1}$  to  $650 \text{ cm}^{-1}$  with a resolution of  $2 \text{ cm}^{-1}$ . These measurements were performed at a single angle of incidence ( $\Phi_a = 70^\circ$ ).

To perform the variable temperature measurements, the  $\text{ThO}_2$  crystal was mounted to an aluminum plate via vacuum seal. To elevate the temperature, the aluminum plate was heated by a pyrolytic boron nitride/pyrolytic graphite resistive heater. The temperature was read before and after each ellipsometric measurement by probing the sample surface with a k-type thermocouple. During the measurement, the thermocouple was removed from the surface.

### IV. RESULTS AND DISCUSSION

#### A. $\text{ThO}_2$ and $\text{UO}_2$ room temperature characterization

In order to characterize the IR-active phonon modes in  $\text{ThO}_2$  and  $\text{UO}_2$ , we implemented the following three-step approach. (i) We apply our optical model and a model dielectric function approach to compare experimental data with best-match model calculated data to obtain the thickness of the surface roughness layer and to identify all IR-active modes. (ii) We extract  $\text{Re}\{\epsilon(\omega)\}$  and  $\text{Im}\{\epsilon(\omega)\}$  for  $\text{ThO}_2$  and  $\text{UO}_2$  for each measured wavelength separately by holding all other optical model parameters constant (surface roughness thickness and  $\text{ThO}_2$  silver contact diameter). (iii) We perform a best-match model calculation using the FPSQ model and by directly comparing the result of the FPSQ model with the wavelength-by-wavelength obtained dielectric function obtained in the second step. In this best-match model calculation, we included evaluations of the match in  $\epsilon(\omega)$  as well as the match in  $\epsilon^{-1}(\omega)$  between the model and wavelength-by-wavelength obtained dielectric function.

Step (i): shown in Fig. 4 is the best-match model calculated ellipsometry data (black solid lines) to the experimental data (dashed lines) for  $\text{ThO}_2$  [panel (a)] and  $\text{UO}_2$  [panel (b)]. The analysis yields a surface roughness layer thickness of  $(34 \pm 1) \text{ nm}$  for  $\text{ThO}_2$  and  $(22 \pm 1) \text{ nm}$  for  $\text{UO}_2$ . In addition to the main mode pair, a small IR-active impurity-like mode pair is detected for both crystals within the reststrahlen band (band of high reflectivity).

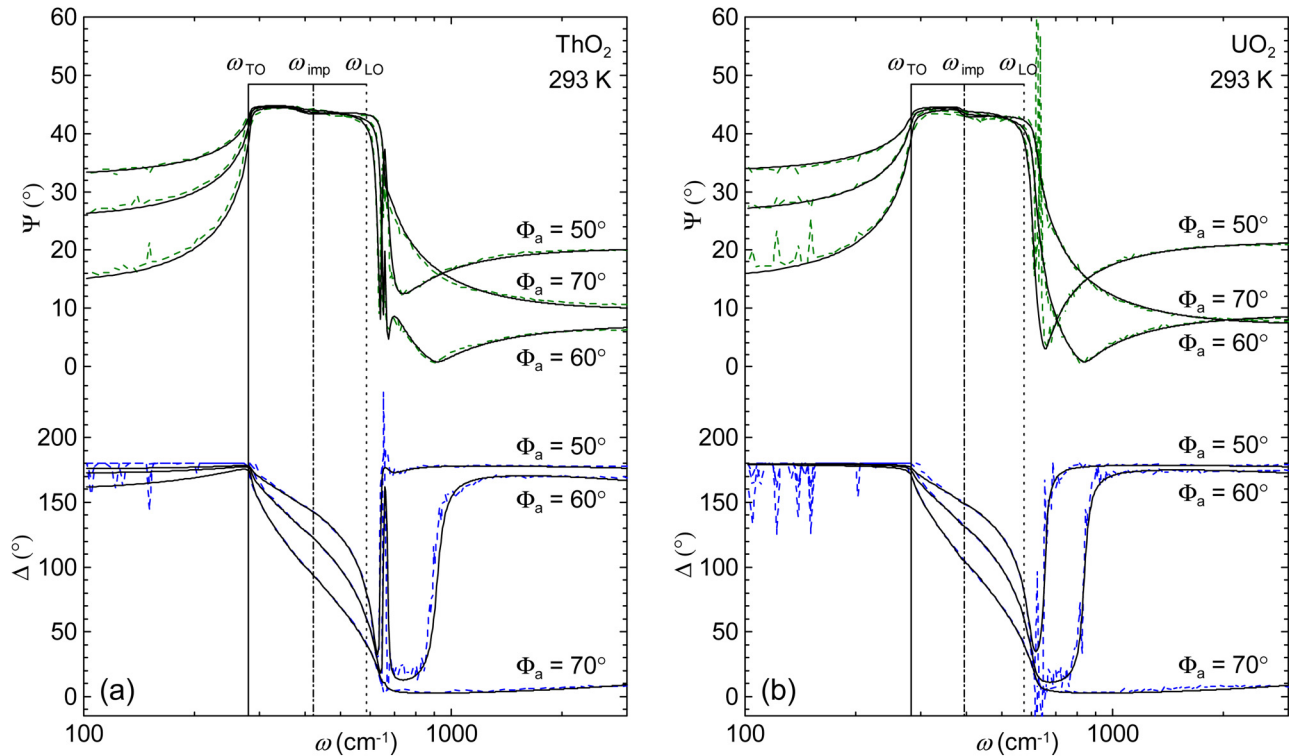


**FIG. 4.** Experimental (dashed lines) and best-match model calculated (black solid lines) ellipsometric data ( $\Psi$ ,  $\Delta$ ) for single-crystal  $\text{ThO}_2$  [panel (a)] and  $\text{UO}_2$  [panel (b)]. The optical model parameters  $\omega_{\text{TO}}$  (solid vertical lines) and  $\omega_{\text{LO}}$  (dashed vertical lines) are the TO and LO frequencies, respectively, that correspond to the main IR-active phonon modes. The parameter  $\omega_{\text{imp}}$  ( $=\omega_{\text{TO,imp}} = \omega_{\text{LO,imp}}$ ) (dashed-dotted vertical lines) corresponds to the small-amplitude IR-active impurity-like mode pair within the reststrahlen band. Data are taken at three angles of incidence ( $\Phi_a = 50^\circ$ ,  $60^\circ$ , and  $70^\circ$ ) and at room temperature.

Because only two mode pairs are observed, we designate the impurity mode pair index as  $i = \text{"imp"}$  and the main mode pair index as null ( $i = \text{""}$ ). We find that there is limited sensitivity to the parameters  $\omega_{\text{TO,imp}}$  and  $\omega_{\text{LO,imp}}$ ; therefore, they were set equal in the model analysis ( $\omega_{\text{imp}} = \omega_{\text{TO,imp}} = \omega_{\text{LO,imp}}$ ), as was done in Ref. 36 for impurity-like modes detected in  $\alpha$ -GaN thin films. In Fig. 4, the impurity mode resonant frequency is labeled as  $\omega_{\text{imp}}$  and the main mode as  $\omega_{\text{TO}}$  and  $\omega_{\text{LO}}$ . The occasional spike-like features in  $\Psi$  and  $\Delta$  (Fig. 4) are due to noise in low-reflectivity spectral ranges. For the  $\text{ThO}_2$ , the small silver contact area was found to be approximately 1% surface coverage of the sample. The analysis verifies that both crystals are optically isotropic for the given temperature and spectral range. No significant contribution from free charge carriers is detected.

Step (ii): shown in Fig. 5 is the wavelength-by-wavelength extracted  $\text{Im}\{\epsilon(\omega)\}$  [panel (a)] and  $\text{Im}\{\epsilon^{-1}(\omega)\}$  [panel (b)] for  $\text{ThO}_2$  (green dashed lines) and  $\text{UO}_2$  (blue dotted lines). The resulting best-match calculated ellipsometry data are virtually indistinguishable from the measured data and are, therefore, not included in Fig. 4.

Step (iii): shown in Fig. 5 is the best-match model dielectric function obtained using the FPSQ model (black solid lines), obtained by direct comparison with the wavelength-by-wavelength

extracted dielectric function. Shown in Table I are the resulting fit parameters for the main mode pair, DFT calculated parameters, and previous results from reflectance spectroscopy. Our results are similar to previous characterizations and our DFT calculations (Fig. 6). For the experiments that report values of  $\gamma_{\text{TO}}$  and  $\gamma_{\text{LO}}$ , it holds true that  $\gamma_{\text{TO}} < \gamma_{\text{LO}}$ . The anharmonicity indicated by  $\gamma_{\text{TO}} \neq \gamma_{\text{LO}}$  is thought to arise from anharmonic coupling between different phonon modes.<sup>13,14,37</sup> The impurity mode pair also exhibits anharmonicity since  $\gamma_{\text{TO,imp}} > \gamma_{\text{LO,imp}}$ . Best-match model results for the impurity mode parameters in both crystals are given in Table II. The anharmonic DFT calculations on  $\text{ThO}_2$  show  $\gamma_{\text{TO}} < \gamma_{\text{LO}}$  as well (Fig. 3). Since our DFT calculations do not consider any impurity modes, this establishes that the anharmonicity in the main phonon mode pair in  $\text{ThO}_2$  is intrinsic to the material and does not depend on the existence of an impurity-like mode pair. However, the existence of impurities could of course influence the phonon properties.

## B. $\text{ThO}_2$ variable temperature characterization

To further investigate  $\text{ThO}_2$ , we performed ellipsometric measurements as a function of temperature from 294 K to 648 K. The spectra acquired at each temperature increment are analyzed



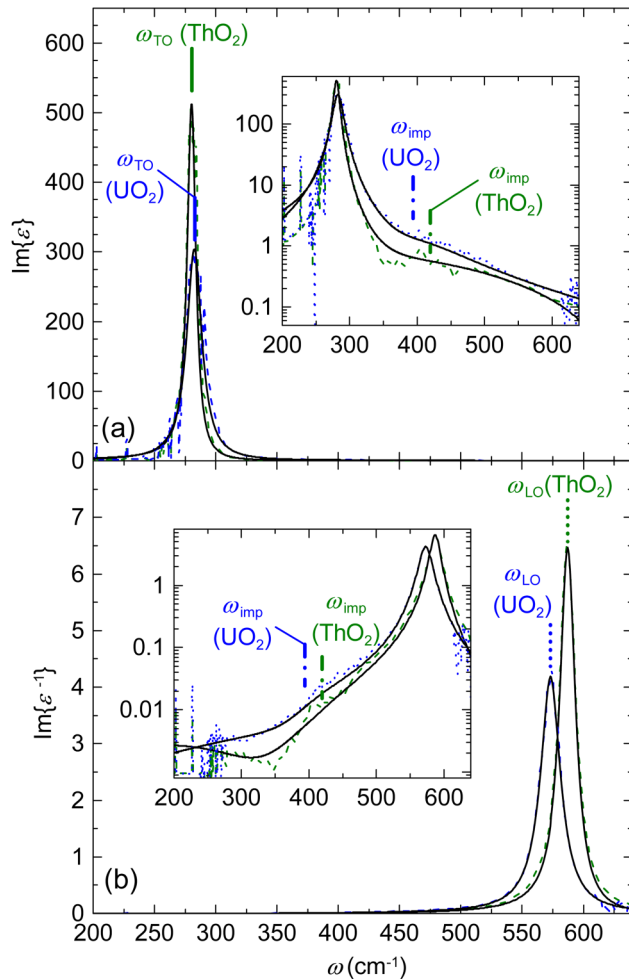


**FIG. 5.** Wavelength-by-wavelength extracted (broken lines) and best-match model calculated (solid black lines)  $\text{Im}\{\varepsilon(\omega)\}$  [panel (a)] and  $\text{Im}\{\varepsilon^{-1}(\omega)\}$  [panel (b)] for single-crystal  $\text{ThO}_2$  (green) and  $\text{UO}_2$  (blue). The solid black lines show the best-match model calculation using Eq. (2) to the wavelength-by-wavelength extracted  $\text{Im}\{\varepsilon(\omega)\}$  and  $\text{Im}\{\varepsilon^{-1}(\omega)\}$ . The resulting best-match model parameters are shown in Tables I and II. The TO and LO resonant frequencies are labeled as  $\omega_{\text{TO}}$  and  $\omega_{\text{LO}}$  for the main phonon mode pair and  $\omega_{\text{imp}}$  ( $=\omega_{\text{TO,imp}} = \omega_{\text{LO,imp}}$ ) for the impurity-like mode pair. To make the impurity mode features visible,  $\text{Im}\{\varepsilon(\omega)\}$  and  $\text{Im}\{\varepsilon^{-1}(\omega)\}$  are also shown on a logarithmic scale (inset plots). Note,  $\omega_{\text{imp}}$  does not exactly coincide with the corresponding peak in  $\text{Im}\{\varepsilon(\omega)\}$  because the impurity mode broadening is comparable to  $\omega_{\text{imp}}$ .

independently and using the model approach described at room temperature. To examine the influence of heat on the surface roughness layer, a separate, variable temperature experiment was performed in the visible spectral range (1.0 eV–6.5 eV, RC2, J.A. Woollam Co., Inc.). No significant change in the roughness layer's thickness or dielectric function was observed. We further assume that the IR optical properties of the small silver contact area remain temperature independent. Therefore, we held these optical model parameters constant as a function of temperature.

Using the approach described previously, we performed a wavelength-by-wavelength fit to extract  $\text{Re}\{\varepsilon(\omega)\}$  and  $\text{Im}\{\varepsilon(\omega)\}$  for each measured temperature. The FPSQ model is then fit to the wavelength-by-wavelength extracted  $\varepsilon(\omega)$  and  $\varepsilon^{-1}(\omega)$  (Fig. 7). The resulting main mode pair and impurity mode pair parameters are shown in Fig. 7. For the main mode pair, the resonant frequency parameters ( $\omega_{\text{TO}}$  and  $\omega_{\text{LO}}$ ) decrease with increasing temperature, whereas the broadening parameters ( $\gamma_{\text{TO}}$  and  $\gamma_{\text{LO}}$ ) increase with increasing temperature, which is a typical behavior for IR-active phonon modes.<sup>40</sup> For the impurity-like mode pair,  $\omega_{\text{imp}}$  decreases with increasing temperature, but interestingly,  $\gamma_{\text{TO,imp}}$  and  $\gamma_{\text{LO,imp}}$  decrease with increasing temperature. This anomalous behavior is discussed in more detail below.

To model the temperature-dependence of the resonant frequencies and broadening parameters, we followed the same approach as in Ref. 16. Similar to Ref. 16, we find that the change in our resonant frequencies is directly proportional to the change in volume of the crystal lattice. The change in resonant frequencies for a given change in volume can be quantified by the mode Grüneisen parameter  $g_j$ , where the index  $j$  specifies the particular lattice resonance (here,  $j=\text{TO}$ ,  $\text{LO}$ , or  $\text{imp}$ ). Assuming a temperature-independent  $g_j$ , the change in the  $j$ th resonant frequency can be written as  $\Delta\omega_j(T) = -\omega_j g_j (\Delta V(T)/V)$ , where  $\omega_j$  is the initial resonant frequency and  $V$  is the lattice volume.<sup>16</sup> This form also assumes that the only change in  $\omega_j(T)$  is due to the lattice expansion. Other temperature-dependent contributions, such as anharmonicity (i.e., the real part of the phonon self-energy), electron-phonon coupling, spin-phonon coupling, etc., were not considered.<sup>13,41</sup> If this model is unable to fit  $\Delta\omega_j(T)$ , this is indicative of other contributions to the frequency shift. To express  $\Delta V(T)/V$  in terms of the linear expansion coefficient  $\alpha_L$  and change in the temperature  $\Delta T$ , we write  $\Delta V(T)/V = 3\alpha_L \Delta T$ , where the volume expansion coefficient  $\alpha_V = 3\alpha_L$  (assuming small differential changes in an isotropic material). Rearranging the prior equation for  $\Delta\omega_j(T)$  to only fit for  $g_j$  yields

$$\omega_j(T) = -\omega_{j,\text{init}}(g_j 3\alpha_L)(T - T_{\text{init}}) + \omega_{j,\text{init}}. \quad (3)$$

Here,  $\omega_{j,\text{init}}$  and  $T_{\text{init}}$  are the initial resonant frequency and temperature [ $\omega_{j,\text{init}} = \omega_j(T_{\text{init}})$ ,  $T_{\text{init}} = 293$  K]. For  $\text{ThO}_2$ , we find that the average linear expansion coefficient in our temperature range is  $\alpha_L = 9.9 \times 10^{-6} \text{ K}^{-1}$ .<sup>42</sup> Fitting Eq. (3) to our results for  $\omega_{\text{TO}}(T)$ ,  $\omega_{\text{LO}}(T)$ , and  $\omega_{\text{imp}}(T)$  gives  $g_{\text{TO}} = 3.3 \pm 0.1$ ,  $g_{\text{LO}} = 0.8 \pm 0.02$ , and  $g_{\text{imp}} = 17.1 \pm 1.0$  [Fig. 7(c)]. The results for  $g_{\text{TO}}$  are in excellent agreement with previous DFT calculations, which predict  $g_{\text{TO}} \approx 3.2$ , only considering volume change effects on the harmonic mode frequency.<sup>5</sup> This suggests that the temperature-induced change in  $\omega_{\text{TO}}$  is primarily due to volume expansion of the crystal lattice, and other temperature-dependent contributions are not significant or perhaps counterbalance each other.<sup>16</sup> However, the  $g_{\text{LO}}$  parameter calculated in Ref. 5 is larger than our experimentally determined value. This could mean that the change in  $\omega_{\text{LO}}$  is due to other temperature-dependent contributions besides a pure volume change. In our anharmonic DFT calculations, performed at a fixed cell volume, i.e., only including the effect of phonon self-energy, the frequency shift of the LO mode has a positive slope (Fig. 3), possibly compensating the effect of the lattice expansion. It is worth noting though that our

**TABLE I.** Best-match model results for the room temperature IR-active phonon mode parameters in single-crystal ThO<sub>2</sub> and UO<sub>2</sub>. Error bars shown for this work correspond to the 90% confidence interval within the best-match model data analysis. The low-frequency (static) dielectric constant  $\epsilon_{DC}$  is calculated using the Lyddane–Sachs–Teller (LST) relation.<sup>38</sup>

Parameter	DFT (this work)	Ellipsometry (this work)		Axe and Pettit <sup>a</sup>		Chernia <sup>b</sup>	Schoenes <sup>c</sup>	DeVetter <i>et al.</i> <sup>d</sup>	Dolling <i>et al.</i> <sup>e</sup>
	ThO <sub>2</sub>	UO <sub>2</sub>	ThO <sub>2</sub>	UO <sub>2</sub>	ThO <sub>2</sub>	UO <sub>2</sub>	UO <sub>2</sub>	UO <sub>2</sub>	UO <sub>2</sub>
$\omega_{TO}$ (cm <sup>-1</sup> )	260	(282.8 ± 0.2)	(280.5 ± 0.1)	(278 ± 2)	(279 ± 2)	283.4	(280 ± 2)	(277 ± 3)	(284 ± 4)
$\omega_{LO}$ (cm <sup>-1</sup> )	554.8	(573.3 ± 0.5)	(587.5 ± 0.2)	(556 ± 4)	(568 ± 4)	574.0	(578 ± 2)	(571 ± 1)	(557 ± 20)
$\gamma_{TO}$ (cm <sup>-1</sup> )	9.0 <sup>f</sup>	(14.8 ± 0.5)	(8.2 ± 0.2)	18.5	16.2	29.4	7.5	...	...
$\gamma_{LO}$ (cm <sup>-1</sup> )	18.4 <sup>f</sup>	(20.1 ± 1.1)	(16.1 ± 0.5)	...	...	30.4	14	...	...
$\epsilon_{\infty}$	4.79	(5.2 ± 0.2)	(4.7 ± 0.1)	5.51	4.86	5.46	5.0	...	...
$\epsilon_{DC}$	21.9	21.1	20.4	21.31	19.71	22.36	21.5	...	...

<sup>a</sup>Reference 7:  $\omega_{TO}$  and  $\omega_{LO}$  from Kramers–Kronig analysis.  $\gamma_{TO}$ ,  $\epsilon_{\infty}$ , and  $\epsilon_{DC}$  from best-match model parameter results using a Lorentz oscillator to render the dielectric function behavior.

<sup>b</sup>Reference 8.

<sup>c</sup>Reference 9.

<sup>d</sup>Reference 10.

<sup>e</sup>Reference 39.

<sup>f</sup>From the anharmonic calculation at 300 K.

calculations only include third order anharmonicity, while fourth order contributions, if present, can in principle be of the same order of magnitude as the third order one, and not necessarily with the same sign, further complicating the picture. For  $\omega_{imp}(T)$ , the trend is not perfectly linear, contrary to what Eq. (3) predicts. This also indicates other mechanisms besides the volume change (Fig. 8).

To investigate the mechanism of anharmonic phonon–phonon scattering, we implement the Bose–Einstein based model for  $\gamma_j(T)$  employed in Ref. 13. Since  $\gamma_{TO}(T)$  and  $\gamma_{LO}(T)$  are reasonably linear within our temperature range, the only term in the equation needed is the one that corresponds to decay via cubic anharmonicities,<sup>16</sup>

$$\gamma_j(T) = a_j \left[ n \left( \frac{\omega_j(T)}{2} \right) + \frac{1}{2} \right], \quad (4)$$

where  $n(\tilde{\omega}) = (e^{\hbar\tilde{\omega}/k_B T} - 1)^{-1}$  is the phonon occupation number evaluated at the average frequency  $\tilde{\omega} = (\omega_j(T)/2)$ . The parameters  $\hbar$ ,  $k_B$ , and  $a_j$  are the reduced Planck constant, the Boltzmann constant, and the cubic anharmonic parameter, respectively.

**TABLE II.** Best-match model results for the room temperature IR-active impurity-like phonon mode parameters in single-crystal ThO<sub>2</sub> and UO<sub>2</sub>. Error bars shown correspond to the 90% confidence interval within the best-match model data analysis.

Parameter	Ellipsometry (this work)	
	UO <sub>2</sub>	ThO <sub>2</sub>
$\omega_{imp}$ (cm <sup>-1</sup> )	(394.3 ± 20.3)	(419.6 ± 11.4)
$\gamma_{TO,imp}$ (cm <sup>-1</sup> )	(143.5 ± 85.5)	(511.9 ± 68.6)
$\gamma_{LO,imp}$ (cm <sup>-1</sup> )	(133.8 ± 80.2)	(443.7 ± 59.5)

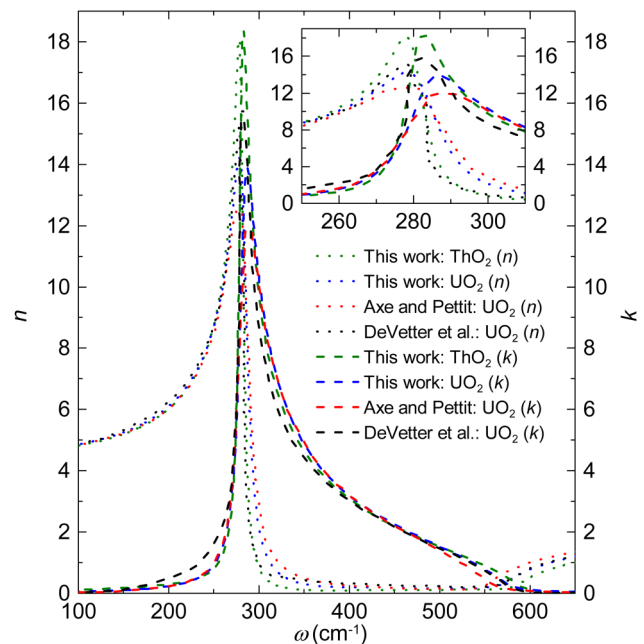


**FIG. 6.** Resulting optical constants  $n$  and  $k$  for the room temperature analysis of ThO<sub>2</sub> and UO<sub>2</sub> compared with other  $n$  and  $k$  values from previous UO<sub>2</sub> characterizations. Optical constants determined in this work [ThO<sub>2</sub> (green lines) and UO<sub>2</sub> (blue lines)] were converted from the best-match model calculated dielectric function shown in Fig. 5. For comparison, dispersion model-calculated optical constants from Axe and Pettit<sup>7</sup> (red lines) were included, as well as values calculated from experimental reflectance spectra by DeVetter *et al.*<sup>10</sup> (black lines). Dotted lines were chosen for  $n$  and dashed lines for  $k$ .

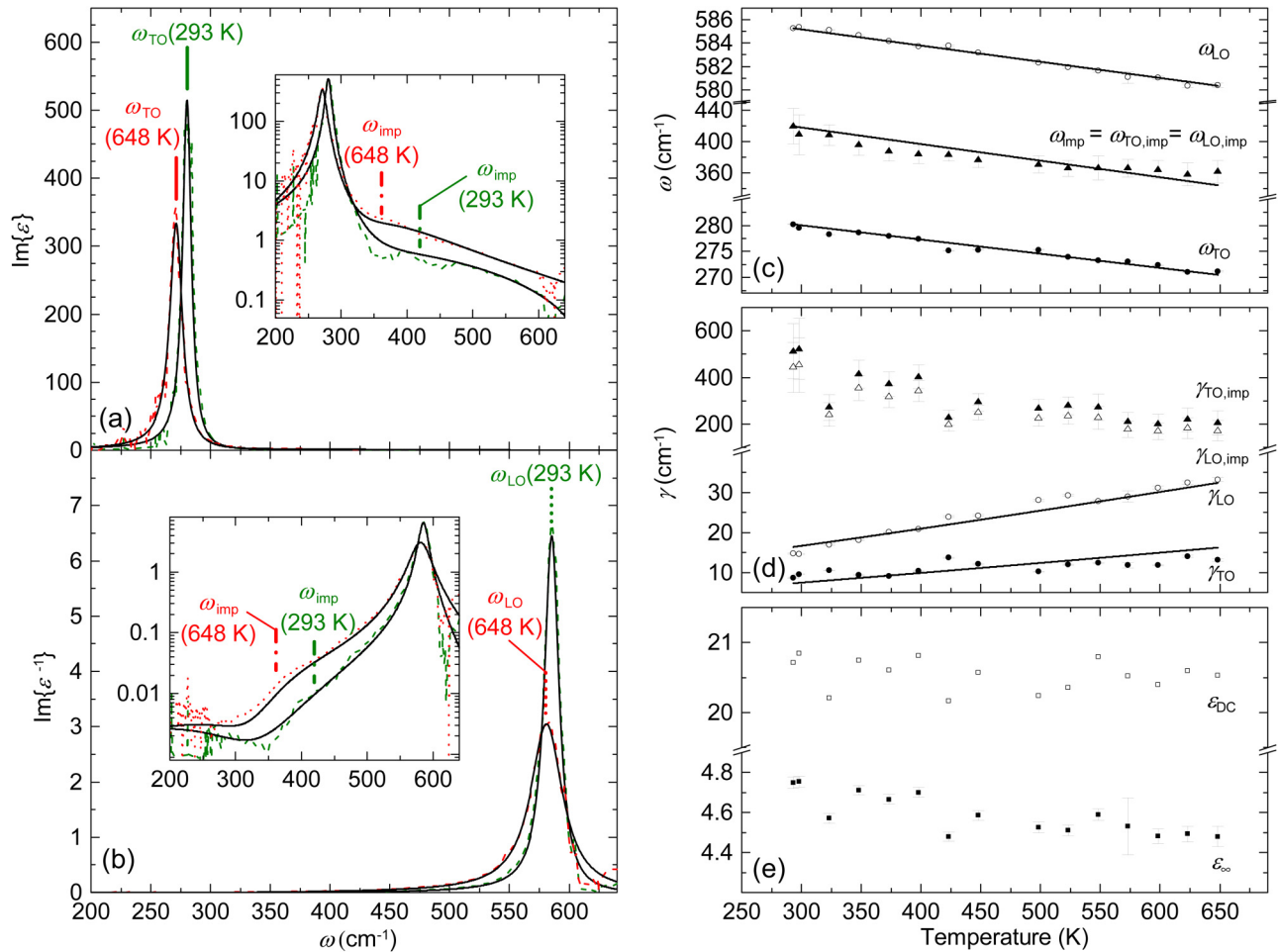


**FIG. 7.** Results for  $\text{ThO}_2$  variable temperature characterization. Wavelength-by-wavelength extracted (broken lines) and best-match model calculated (solid black lines)  $\text{Im}\{\epsilon(\omega)\}$  [panel (a)] and  $\text{Im}\{\epsilon^{-1}(\omega)\}$  [panel (b)] for single-crystal  $\text{ThO}_2$  at 293 K (green) and 648 K (red). To make the impurity mode features visible,  $\text{Im}\{\epsilon(\omega)\}$  and  $\text{Im}\{\epsilon^{-1}(\omega)\}$  are also shown on a logarithmic scale [inset plots in panels (a) and (b)]. The solid black lines in panels (a) and (b) show the best-match model results of Eq. (2) to the wavelength-by-wavelength extracted  $\text{Im}\{\epsilon(\omega)\}$  and  $\text{Im}\{\epsilon^{-1}(\omega)\}$ . The resulting FPSQ model parameters for all measured temperatures are shown in panels (c)–(e). The low-frequency (static) dielectric constant  $\epsilon_{\text{DC}}$  is calculated using the Lyddane–Sachs–Teller (LST) relation.<sup>38</sup> The solid black lines in panel (c) show the best-match model results using Eq. (3) to match  $\omega_j(T)$ . The solid black lines in panel (d) show the best-match model using Eq. (4) for  $\gamma_j(T)$ .

Fitting Eq. (4) to  $\gamma_{\text{TO}}(T)$  and  $\gamma_{\text{LO}}(T)$  gives  $a_{\text{TO}} = (4.8 \pm 0.2) \text{ cm}^{-1}$  and  $a_{\text{LO}} = (20.2 \pm 0.4) \text{ cm}^{-1}$ . Our anharmonic DFT calculated results for  $\gamma_{\text{TO}}(T)$  and  $\gamma_{\text{LO}}(T)$  (Fig. 3) give similar fit parameter results of  $a_{\text{TO}} = (5.7 \pm 0.1) \text{ cm}^{-1}$  and  $a_{\text{LO}} = (21.3 \pm 0.6) \text{ cm}^{-1}$ . A larger temperature range is used when fitting the DFT results (0 K–800 K) than for our ellipsometry results (293 K–648 K). However, the  $a_{\text{TO}}$  and  $a_{\text{LO}}$  for DFT are nearly identical when only including data within the range of 293 K–648 K. We can then conclude that the dominant decay mechanism can be described as phonon–phonon interactions via cubic anharmonicities.<sup>17</sup> It is worth noting that Eq. (4) was introduced in Ref. 13 to describe the decay of optical phonons into pairs of acoustic phonons via cubic anharmonicities, while the anharmonic DFT code considers a more

complex decay mechanism involving triplets of phonons at arbitrary wavevectors over a fine grid of q-points within the Brillouin zone (in our case on a grid of  $200 \times 200 \times 200$  points). Equation (4), however, describes thermal occupations of phonon states within the Bose–Einstein statistics and hence should be applicable in either case.

Interestingly,  $\gamma_{\text{TO,imp}}(T)$  and  $\gamma_{\text{LO,imp}}(T)$  decrease with increasing temperature. This dependence cannot be fit by the model in Ref. 13 and is not typical for IR-active phonon modes in pure crystals.<sup>40</sup> However, the temperature-dependence of impurity-like modes is not well understood. While the exact nature of the impurity mode is unclear, it may be a result of subtle anharmonic phonon–phonon interactions, as reported for  $\text{MgO}$ .<sup>43</sup> This, however, falls outside the scope of our current study.

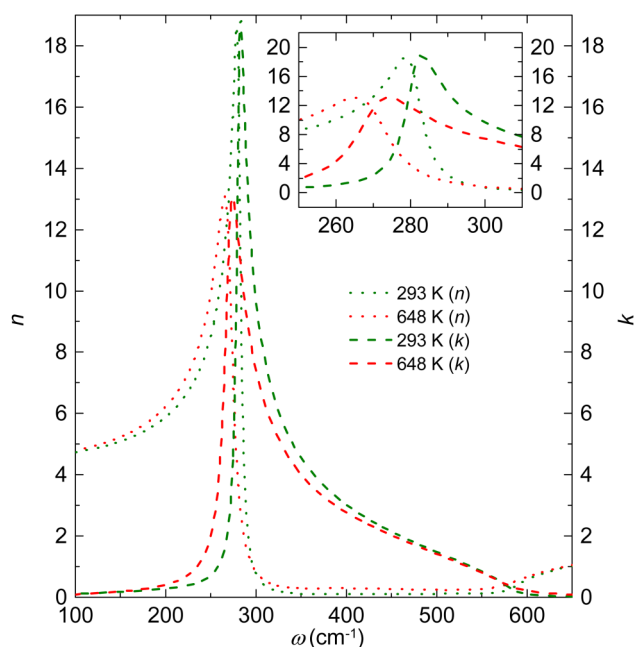


**FIG. 8.** Resulting optical constants  $n$  and  $k$  for the variable temperature characterization of  $\text{ThO}_2$ . Optical constants (green for 293 K and red for 648 K) were determined by converting the best-match model calculated dielectric function shown in Fig. 7. Dotted lines are chosen for  $n$  and dashed lines for  $k$ .

## V. CONCLUSION

In summary, IRSE experiments and DFT calculations were used to study the IR-active phonon modes in  $\text{ThO}_2$  and  $\text{UO}_2$ . Their dielectric functions are extracted from the ellipsometric data in order to determine the phonon mode resonant frequency and broadening parameters. In agreement with previous results, we find  $\gamma_{\text{TO}} < \gamma_{\text{LO}}$  for both crystals, which is indicative of lattice anharmonicity due to anharmonic interactions between phonon modes. For  $\text{ThO}_2$ , additional ellipsometric measurements were performed at elevated temperatures. For the main TO resonance, our experimentally determined results for the mode Grüneisen parameter are in excellent agreement with previous DFT calculations, which suggests that the temperature-induced change in the TO resonant frequency is due to volume expansion of the crystal lattice. However, the mode Grüneisen parameter for the main LO resonance does not exactly match the DFT predictions. This indicates that the temperature-dependence of the LO resonant frequency is determined by additional factors besides just a volume change. By implementing the Bose–Einstein based model in Ref. 13 to describe the broadening’s temperature-dependence, we find that the decay mechanism of the main mode’s IR-active phonons can be described as cubic anharmonicity. For the detected impurity-like mode pair, the broadening parameters decrease with increasing temperature. This behavior is not predicted by the Bose–Einstein model, and more investigation is needed to understand temperature-dependence of the impurity-like modes.

## ACKNOWLEDGMENTS

This work was supported in part by the National Science Foundation (NSF) under Award No. DMR 1420645 (Nebraska Materials Research Science and Engineering Center) and under Award No. DMR 1808715. This work was supported in part by the Air Force Office of Scientific Research (AFOSR) under Award No. FA9550-18-1-0360 and by the Defense Threat Reduction Agency (Grant No. HDTRA1-14-1-0041) and the Domestic Nuclear Detection Office of the Department of Homeland Security (Grant No. HSHQDC14X00089). J.M.M. was supported by the Center for Thermal Energy Transport under Irradiation, an Energy Frontier Research Center funded by the U.S. Department of Energy, Office of Science, Office of Basic Energy Sciences. S.K., R.K., A.M., and M.S. acknowledge partial support by the J. A. Woollam Foundation. Density functional theory calculations were performed at the Holland Computing Center at the University of Nebraska, which receives support from the Nebraska Research Initiative. The views expressed in this article are those of the authors and do not necessarily reflect the official policy or position of the United States Air Force, Department of Defense, or the U.S. Government.

## REFERENCES

- M. Lyons, R. Boyle, J. Davies, V. Hazel, and T. Rowland, *Nucl. Eng. Des.* **21**, 167 (1972).
- B. Frost, *R. Inst. Chem. Rev.* **2**, 163 (1969).
- J. W. Pang, W. J. Buyers, A. Chernatynskiy, M. D. Lumsden, B. C. Larson, and S. R. Phillpot, *Phys. Rev. Lett.* **110**, 157401 (2013).
- Q. Yin and S. Y. Savrasov, *Phys. Rev. Lett.* **100**, 225504 (2008).
- Y. Lu, Y. Yang, and P. Zhang, *J. Phys. Condens. Matter* **24**, 225801 (2012).
- M. Schubert, *Infrared Ellipsometry on Semiconductor Layer Structures: Phonons, Plasmons, and Polaritons* (Springer Science & Business Media, 2004), Vol. 209.
- J. Axe and G. Pettit, *Phys. Rev.* **151**, 676 (1966).
- Z. Chernia, *Phys. Chem. Chem. Phys.* **11**, 1729 (2009).
- J. Schoenes, *Phys. Rep.* **63**, 301 (1980).
- B. M. DeVetter, T. L. Myers, B. D. Cannon, N. K. Scharko, M. R. K. Kelly-Gorham, J. F. Corbey, A. L. Schemer-Kohrn, C. T. Resch, D. D. Reilly, and T. J. Johnson, *J. Phys. Chem. A* **122**, 7062 (2018).
- H. Fujiwara, *Spectroscopic Ellipsometry: Principles and Applications* (John Wiley & Sons, 2007).
- R. M. A. Azzam and N. M. Bashara, *Ellipsometry and Polarized Light* (North-Holland, Elsevier Science Publishing Co., Inc., 1987).
- F. Gervais and B. Piriou, *J. Phys. C: Solid State Phys.* **7**, 2374 (1974).
- F. Gervais, *Solid State Commun.* **13**, 1211 (1973).
- F. Gervais and B. Piriou, *Phys. Rev. B* **10**, 1642 (1974).
- F. Gervais and B. Piriou, *Phys. Rev. B* **11**, 3944 (1975).
- P. Klemens, *Phys. Rev.* **148**, 845 (1966).
- Quantum ESPRESSO is available from <http://www.quantum-espresso.org>;
- P. Giannozzi, S. Baroni, N. Bonini, M. Calandra, R. Car, C. Cavazzoni, D. Ceresoli, G. L. Chiarotti, M. Cococcioni, I. Dabo, A. D. Corso, S. de Gironcoli, S. Fabris, G. Fratesi, R. Gebauer, U. Gerstmann, C. Gougoussis, A. Kokalj, M. Lazzeri, L. Martin-Samos, N. Marzari, F. Mauri, R. Mazzarello, S. Paolini, A. Pasquarello, L. Paulatto, C. Sbraccia, S. Scandolo, G. Sclauzero, A. P. Seitsonen, A. Smogunov, P. Umari, and R. M. Wentzcovitch, *J. Phys.: Cond. Mat.* **21**, 395502 (2009).
- J. P. Perdew, K. Burke, and M. Ernzerhof, *Phys. Rev. Lett.* **77**, 3865 (1996).
- PSLibrary available from <https://dalcorsogithub.io/pslibrary/>; A. D. Corso, *Comput. Mater. Sci.* **95**, 337 (2014).
- H. J. Monkhorst and J. D. Pack, *Phys. Rev. B* **13**, 5188 (1976).

- <sup>22</sup>S. Baroni, S. de Gironcoli, A. D. Corso, S. Baroni, S. de Gironcoli, and P. Giannozzi, *Rev. Mod. Phys.* **73**, 515 (2001).
- <sup>23</sup>W. Setyawan and S. Curtarolo, *Comput. Mat. Sci.* **49**, 299 (2010).
- <sup>24</sup>M. Born and K. Huang, *Dynamical Theory of Crystal Lattices* (Clarendon Press, Oxford, 1954).
- <sup>25</sup>G. Venkataraman, L. A. Feldkamp, and V. C. Sahni, *Dynamics of Perfect Crystals* (MIT Press, 1975).
- <sup>26</sup>X. Gonze and C. Lee, *Phys. Rev. B* **55**, 10355 (1997).
- <sup>27</sup>A. Kokalj, *Comp. Mater. Sci.* **28**, 155 (2003), code available at <http://www.xcrysden.org>.
- <sup>28</sup>M. Lazzeri and S. de Gironcoli, *Phys. Rev. Lett.* **81**, 2096 (1998).
- <sup>29</sup>N. Bonini, M. Lazzeri, N. Marzari, and F. Mauri, *Phys. Rev. Lett.* **99**, 176802 (2007).
- <sup>30</sup>L. Paulatto, F. Mauri, and M. Lazzeri, *Phys. Rev. B* **87**, 214303 (2013).
- <sup>31</sup>D. Vanderbilt, *Phys. Rev. B* **32**, 8412 (1985).
- <sup>32</sup>J. P. Perdew and A. Zunger, *Phys. Rev. B* **23**, 5048 (1981).
- <sup>33</sup>A. Mock, C. Dugan, S. Knight, R. Korlacki, J. M. Mann, M. M. Kimani, J. C. Petrosky, P. A. Dowben, and M. Schubert, *Appl. Phys. Lett.* **114**, 211901 (2019).
- <sup>34</sup>C. L. Dugan, G. G. Peterson, A. Mock, C. Young, J. M. Mann, M. Nastasi, M. Schubert, L. Wang, W.-N. Mei, I. Tanabe *et al.*, *Eur. Phys. J. B* **91**, 67 (2018).
- <sup>35</sup>P. Kühne, C. M. Herzinger, M. Schubert, J. A. Woollam, and T. Hofmann, *Rev. Sci. Instrum.* **85**, 071301 (2014).
- <sup>36</sup>A. Kasic, M. Schubert, S. Einfeldt, D. Hommel, and T. Tiwald, *Phys. Rev. B* **62**, 7365 (2000).
- <sup>37</sup>M. Schubert, T. Tiwald, and C. Herzinger, *Phys. Rev. B* **61**, 8187 (2000).
- <sup>38</sup>R. H. Lyddane, R. G. Sachs, and E. Teller, *Phys. Rev.* **59**, 673 (1941).
- <sup>39</sup>G. Dolling, R. Cowley, and A. Woods, *Can. J. Phys.* **43**, 1397 (1965).
- <sup>40</sup>A. S. Mikheykin, E. S. Zhukova, V. I. Torgashev, A. G. Razumnaya, Y. I. Yuzuyuk, B. P. Gorshunov, A. S. Prokhorov, A. E. Sashin, A. A. Bush, and M. Dressel, *Eur. Phys. J. B* **87**, 232 (2014).
- <sup>41</sup>P. Kumar, S. Saha, C. Serrao, A. Sood, and C. Rao, *Pramana* **74**, 281 (2010).
- <sup>42</sup>T. Yamashita, N. Nitani, T. Tsuji, and H. Inagaki, *J. Nucl. Mater.* **245**, 72 (1997).
- <sup>43</sup>P. Giura, L. Paulatto, F. He, R. P. Lobo, A. Bosak, E. Calandrini, L. Paolasini, and D. Antonangeli, *Phys. Rev. B* **99**, 220304 (2019).